

1 **Technical note: Measurement of chemically-resolved volume**
2 **equivalent diameter and effective density of particles by AAC-**
3 **SPAMS**

4 Long Peng^{1,2}, Lei Li⁴, Guohua Zhang^{1, 3*}, Xubing Du⁴, Xinming Wang^{1, 3}, Ping'an
5 Peng^{1, 3}, Guoying Sheng¹, Xinhui Bi^{1, 3*}

6

7 ¹ State Key Laboratory of Organic Geochemistry and Guangdong Provincial Key
8 Laboratory of Environmental Protection and Resources Utilization, Guangzhou
9 Institute of Geochemistry, Chinese Academy of Sciences, Guangzhou 510640, China

10 ² University of Chinese Academy of Sciences, Beijing, 100049, China

11 ³ Guangdong-Hong Kong-Macao Joint Laboratory for Environmental Pollution and
12 Control, Guangzhou 510640, China

13 ⁴ Institute of Mass Spectrometer and Atmospheric Environment, Jinan University,
14 Guangzhou 510632, China

15

16 *Correspondence to: bixh@gig.ac.cn and zhanggh@gig.ac.cn

17 **Abstract**

18 Size and effective density (ρ_e) are important properties of aerosol particles and are
19 related to their influences on human health and the global climate. The volume
20 equivalent diameter (D_{ve}) is an intrinsic property that is used to evaluate particle size.
21 ρ_e , defined as the ratio of particle density to a dynamic shape factor (χ), is used to
22 characterize the physical property of a particle as an alternative to particle density.
23 However, it is still challenging to simultaneously characterize the D_{ve} and ρ_e of particles.
24 Here, we present a novel system that classifying particles with their aerodynamic
25 diameter (D_a) by aerodynamic aerosol classifiers (AAC) and determining their vacuum
26 aerodynamic diameter (D_{va}) by single particle aerosol mass spectrometry (SPAMS) to
27 achieve a measurement of D_{ve} and ρ_e . The reliability of the AAC-SPAMS system for
28 accurately obtaining D_{ve} and ρ_e is verified based on the results that the deviation between
29 the measured values and the theoretical values is less than 6% for the size-resolved
30 spherical polystyrene latex (PSL). The AAC-SPAMS system is applied to characterize
31 the D_{ve} and ρ_e of $(\text{NH}_4)_2\text{SO}_4$ and NaNO_3 particles, suggesting that these particles are
32 aspherical and their ρ_e are independent of particle size. Finally, the AAC-SPAMS
33 system is deployed in a field measurement, showing that it is a powerful technique to
34 characterize the chemically-resolved D_{ve} and ρ_e of particles in real time.

35 1. Introduction

36 Size and particle density (ρ_p) are critical parameters of aerosol particles in
37 quantifying the impact of aerosols on air quality, human health and global climate
38 change (Buseck and Posfai, 1999; Poschl, 2005; Pitz et al., 2003). Effective density (ρ_e)
39 has been adopted to characterize the physical property of a particle as an alternative to
40 ρ_p , since ρ_p for aspherical aerosol particles is hardly measured (Sumlin et al., 2018;
41 Katrib et al., 2005). Size and ρ_e govern the transport properties of a particle both in the
42 atmosphere and in the human respiratory system (Seinfeld and Pandis, 1998; Liu and
43 Daum, 2008) and directly/indirectly influence the potential of the particle to absorb or
44 reflect solar radiation (Tang, 1997; Zhao et al., 2019; Liu and Daum, 2008). ρ_e can also
45 provide information concerning particle morphology (Yon et al., 2015) and serve as a
46 tracer for atmospheric processing (Guo et al., 2014; Yin et al., 2015; Liu et al., 2015).
47 However, the quantitative relationship between aerosol properties, namely, size and ρ_e ,
48 and their effects on air quality, human health and global climate change is not yet well
49 understood, which is partly because important aerosol properties cannot be measured
50 by current techniques.

51 **Size.** Size is a fundamental property of particles, which can be parameterized by the
52 physical quantity of volume equivalent diameter (D_{ve}). Defined as the diameter of a
53 spherical particle with the same volume as the particle (DeCarlo et al., 2004), D_{ve} is an
54 intrinsic physical quantity that can be used to evaluate the actual size of the particle.
55 However, to date, atmospheric science usually describes particle size by other diameter
56 definitions, such as the electric mobility diameter (D_m), aerodynamic equivalent

57 diameter (D_a) and vacuum aerodynamic equivalent diameter (D_{va}), whose relationships
 58 with D_{ve} are shown in Eqs. (1)-(3), respectively:

$$59 \quad \frac{D_m}{C_c(D_m)} = \frac{D_{ve}}{C_c(D_{ve})} \chi_t, \quad (1)$$

$$60 \quad D_a = D_{ve} \sqrt{\frac{\rho_p C_c(D_{ve})}{\chi_t \rho_0 C_c(D_a)}}, \quad (2)$$

$$61 \quad D_{va} = \frac{\rho_p D_{ve}}{\rho_0 \chi_v}, \quad (3)$$

62 where $C_c(D)$ is the Cunningham slip correction factor, χ_t and χ_v represent the aerosol
 63 dynamic shape factor (χ) in the transition regime and in the free-molecule regime,
 64 respectively, and ρ_0 represents the unit density of 1.0 g/cm³. From the definitions, it can
 65 be seen that D_m , D_a , and D_{va} are originally derived from D_{ve} , but in actuality, they do
 66 not reflect the actual size of the particle. Meanwhile, D_{ve} cannot be easily obtained,
 67 which limits its application in the scientific community.

68 **Effective density.** At present, three definitions of ρ_e are introduced in atmospheric
 69 science (DeCarlo et al., 2004): the first definition (ρ_e^I) is the ratio of the measured
 70 particle mass (m_p) to the particle volume (V) calculated assuming a spherical particle
 71 with a diameter equal to the measured D_m ; the second definition (ρ_e^{II}) is the ratio of ρ
 72 to χ (Hand and Kreidenweis, 2002); and the third definition (ρ_e^{III}) is the ratio of D_m and
 73 D_{va} , all of which are expressed in Eqs. (4)-(6), respectively.

$$74 \quad \rho_e^I = \frac{6m_p}{\pi D_m^3} \quad (4)$$

$$75 \quad \rho_e^{II} = \frac{\rho_p}{\chi} \quad (5)$$

$$76 \quad \rho_e^{III} = \frac{D_{va}}{D_m} \rho_0 \quad (6)$$

77 The definitions of ρ_e^I and ρ_e^{III} can be derived into the final forms, as shown in the Eqs.(7)
 78 and (8), respectively.

79
$$\rho_e^I = \frac{\rho}{\chi t^3} \cdot \left(\frac{C_c(D_{ve})}{C_c(D_m)} \right)^3 \quad (7)$$

80
$$\rho_e^{III} = \rho \cdot \frac{C_c(D_{ve})}{\chi^2 \cdot C_c(D_m)} \quad (8)$$

81 The Eq. (7) is derived from combining the Eq. (1) with Eq. (4) in which m_p is equal to
 82 $1/6 \rho \cdot D_{ve}^3$. The detailed derivation of Eq. (8) was presented in Schneider et al. (2006). A
 83 variety of methods are developed to characterize ρ_e^I and ρ_e^{III} , among which the more
 84 advanced methods are to achieve the measurement of the chemically-resolved effective
 85 density. Combining a single particle soot photometer (SP2) with a (volatility) tandem
 86 differential mobility analyser ((VT)DMA) can measure the ρ_e^I of particles mixed with
 87 soot (Zhang et al., 2016b; Wu et al., 2019; Han et al., 2019). The measurement of
 88 chemically-resolved ρ_e^{III} can be achieved by coupling a DMA with an on-line aerosol
 89 mass spectrometer including the single particle laser ablation time-of-flight mass
 90 spectrometer (SPLAT I/II) (Zelenyuk et al., 2005; Zelenyuk et al., 2006; Alexander et
 91 al., 2016), aerosol mass spectrometer (AMS) (Dinar et al., 2006; Schneider et al., 2006;
 92 Kiselev et al., 2010), aerosol time-of-flight mass spectrometer (ATOFMS) (Spencer and
 93 Prather, 2006; Spencer et al., 2007), and single-particle aerosol mass spectrometry
 94 (SPAMS) (Zhang et al., 2016a; Zhai et al., 2017). However, the ρ_e^I and ρ_e^{III} are
 95 demonstrated to have the inherent characteristics of decreasing with increasing particle
 96 size (Eqs. (7) and (8)) in a separate paper. Therefore, it will introduce systemic error
 97 when assessing the particle impacts on visibility, human health and climate from the
 98 physical quantities in ρ_e^I and ρ_e^{III} . In contrast, ρ_e^{II} is independent of particle size.
 99 Previously, ρ_e^{II} and the real part in the refractive index (n) can be retrieved from a fitting
 100 procedure that compares the measured light-scattering intensity of particles (R_{meas}) to

101 the theoretical values ($R_{theory,test}$) calculated by a series of n and ρ_e^{II} values. Moffet and
102 Prather (2005) successfully obtained ρ_e^{II} for spherical particles by single particle mass
103 spectrometry. However, subject to the accuracy of Mie theory for the aspherical
104 particles, dry NaCl and calcium-rich dust particles were failed to fit the $R_{theory,test}$ well
105 to R_{meas} (Moffet et al., 2008). Similarly, Zhang et al. (2016a) failed to simultaneously
106 retrieve ρ_e^{II} and n for $(NH_4)_2SO_4$ and $NaNO_3$ particles. To our best knowledge, there is
107 no effective technique to achieve the measurement of ρ_e^{II} for aspherical particles. For
108 reference, the symbol ρ_e in the following text refers to the definition of ρ_e^{II} .

109 The aim of the present work is to develop a method to simultaneously obtain D_{ve} and
110 ρ_e . The established system of an aerodynamic aerosol classifier (AAC)-SPAMS is
111 capable of characterizing the D_a and D_{va} of particles, which can be applied to
112 theoretically derive D_{ve} and ρ_e . To verify the reliability of the AAC-SPAMS system, we
113 apply it to measure the D_{ve} and ρ_e of the spherical particles of polystyrene latex (PSL).
114 The results are in good agreement with the theoretical values. Finally, the AAC-SPAMS
115 system is applied to measure the D_{ve} and ρ_e for $(NH_4)_2SO_4$ and $NaNO_3$ particles and for
116 the chemically-resolved atmospheric particles.

117

118 **2. Experimental section**

119 **2.1 Measurement system**

120 Figure 1 shows a schematic diagram of the AAC-SPAMS system. The particles are
121 first dried by a diffusion drying tube (TSI 9302, USA), classified by AAC (Cambustion
122 Ltd., UK) based on the aerodynamic diameters D_a , and then transported into SPAMS in

123 which the D_{va} and the mass spectra of individual particles are obtained. The working
124 principle of the AAC is described in detail elsewhere (Tavakoli and Olfert, 2013). AAC
125 consists of two coaxial cylinders that rotate at the same rotational speed. Polydisperse
126 particles enter into the space between the cylinders (i.e., classification column) and
127 experience a centrifugal force that causes them to move toward the outer cylinder. The
128 particles to be classified can leave the classification column with the particle-free sheath
129 flow and finally exit the AAC with the sample flow. Thus, the D_a values of classified
130 particles can be derived from their relationship with their relaxation time (τ), as shown
131 in Eq. (9):

$$132 \quad \tau = \frac{c_c(D_a) \cdot \rho_0 \cdot D_a^2}{18\mu} \quad (9)$$

133 where μ is the gas dynamic viscosity. Particles with large relaxation times impact and
134 adhere to the outer cylinder, while particles with small relaxation times exit the
135 classifier with the exhaust flow. The exhaust flow from the AAC was about 0.3 lpm,
136 and the Size Resolution Parameter (Rs) of the AAC was set as 40.

137 Detailed information about the operation of SPAMS (Hexin Analytical Instrument
138 Co., Ltd., China) is described elsewhere (Li et al., 2011). Briefly, the particles are
139 introduced into the vacuum system through a 0.1 mm critical orifice and are gradually
140 collimated into a beam in the aerodynamic lens. Two continuous diode Nd:YAG laser
141 beams (532 nm) are used to aerodynamically size the particles, which are subsequently
142 desorbed/ionized by a pulsed laser (266 nm) that is triggered based on the velocity of a
143 specific particle. The generated positive and negative ions are recorded with the
144 corresponding particle size. The D_{va} of the particle is related to the transit time between

145 the two laser beams (532 nm) in SPAMS, which can be obtained by using a calibration
146 curve generated from the measured transit times of a PSL series with predefined sizes
147 (nominal diameters).

148

149 **2.2 Laboratory experiments**

150 Dried spherical PSL (Nanosphere Size Standards, Duke Scientific Corp., Palo Alto)
151 ($\rho_p = 1.055 \text{ g/cm}^3$ and $\chi = 1.0$) with D_{ve} values of $203 \pm 5 \text{ nm}$, $310 \pm 6 \text{ nm}$, $510 \pm 5 \text{ nm}$,
152 and $740 \pm 6 \text{ nm}$ were used in the AAC-SPAMS system, and the D_{ve} was verified by
153 Scanning Mobility Particles Sizer (Model 3938, TSI Inc., USA). The PSL particles were
154 first classified by AAC, and then their D_{va} values were obtained by SPAMS. ACC-
155 SPAMS was also applied to the particles of $(\text{NH}_4)_2\text{SO}_4$ ($\rho_p = 1.77 \text{ g/cm}^3$) and NaNO_3
156 ($\rho_p = 2.26 \text{ g/cm}^3$) with D_a values of 250.0 nm, 350.0 nm, 450.0 nm and 550.0 nm.
157 Besides, to present the measurement uncertainty of the AAC, the D_a values of these
158 PSL particles were measured to be 212.8 ± 0.2 , 324.7 ± 0.4 , 529.9 ± 0.4 , and $767.5 \pm$
159 0.4 , respectively, by the system of AAC- condensation particle counter (CPC), which
160 shows that the AAC has the deviations of 1.1%, 1.3%, 0.8%, and 0.7% for determining
161 the D_a values of the particles.

162 **2.3 Ambient sampling**

163 For field observations, the AAC-SPAMS system was placed in science and
164 technology enterprise accelerator A2 Block, Guangzhou, China, to characterize the D_{ve} ,
165 ρ_e and chemical compositions of aerosol particles. The sampling inlet was hung 2.5
166 meters from the third floor ($\sim 12 \text{ m}$ above ground level). Ambient aerosol particles were

167 introduced into the AAC through a 5 m long conductive silicone tube with an inner
 168 diameter of 6 mm and a PM_{2.5} cyclone inlet. The sampling flow from the PM_{2.5} cyclone
 169 inlet was 3 lpm, and the residence time in the conductive silicone tube was
 170 approximately 5 seconds. Sampled particles were classified by the AAC as one of four
 171 D_a : 250.0 nm, 350.0 nm, 450.0 nm and 550.0 nm. The sampling time for the particles
 172 of each D_a was approximately 10 minutes. From July 6th to 8th, 2019, approximately
 173 129,869 ionized particles were obtained from nine rounds of measurement. The
 174 sampling details are shown in Table S1. The number of ionized particles with the D_a of
 175 250.0, 350.0, 450.0, and 550.0 nm is about 35,609, 38,374, 31,910, and 23,976,
 176 respectively. The sampled ~100,000 particles are first classified by using an adaptive
 177 resonance theory neural network (ART-2a) (Song et al., 1999) with a vigilance factor
 178 of 0.75, a learning rate of 0.05 and 20 iterations.

179

180 **2.4 Theoretical derivation of D_{ve} and ρ_e from D_a and D_{va}**

181 D_{ve} is the accurate physical quantity of the size of a particle. ρ_e is an alternative
 182 property for ρ_p , which is consistent with the property of ρ_p in terms of being independent
 183 of particle size. These two properties cannot yet be simultaneously measured for
 184 unknown particles by current techniques. In this study, the calculations of D_{ve} and ρ_e for
 185 unknown particles are theoretically derived from D_a and D_{va} . Combining Eqs. (2) and
 186 (3), we obtain the following Eq. (10):

$$187 \quad C_c(D_a) \frac{D_a^2}{D_{va}} = D_{ve} C_c(D_{ve}) \frac{\chi_v}{\chi_t} \quad (10)$$

188 Based on the approximation between χ_v and χ_t ($\chi_v \approx \chi_t = \chi_a$) (DeCarlo et al., 2004), Eq.

189 (10) becomes Eq. (11):

$$190 \quad C_c(D_a) \frac{D_a^2}{D_{va}} = D_{ve} C_c(D_{ve}) \quad (11)$$

191 The Cunningham Slip Correction Factor is calculated by Eq. (12) (DeCarlo et al., 2004):

$$192 \quad C_c(D) = 1 + \frac{\lambda}{D} \left(A + B \cdot \exp\left(\frac{C \cdot D}{\lambda}\right) \right), \quad (12)$$

193 where λ is the mean free path of the gas molecules, and A , B and C are empirically

194 determined constants specific to the analysis system. The values of A , B and C are 2.33,

195 0.966, and -0.498, respectively, which are provided by the manual of the AAC.

196 Substituting Eq. (12) into Eq. (11) obtains the Eq. (13).

$$197 \quad \frac{D_a^2}{D_{va}} + \frac{D_a \cdot \lambda}{D_{va}} \left(A + B \cdot \exp\left(\frac{C \cdot D_a}{\lambda}\right) \right) = D_{ve} + \lambda \left(A + B \cdot \exp\left(\frac{C \cdot D_{ve}}{\lambda}\right) \right) \quad (13)$$

198 Thus, if the D_a and D_{va} of an unknown particle can be measured, its D_{ve} will be

199 calculated according to Eq. (13). Finally, the ρ_e value of the particles is calculated by

200 the D_{va} and D_{ve} values according to Eq. (14), which is obtained by combining Eq.(3)

201 and Eq.(5):

$$202 \quad \rho_e = \frac{\rho_p}{\chi_a} = \frac{D_{va}}{\rho_0 \cdot D_{ve}} \quad (14)$$

203 Thus, we can obtain both the D_{ve} and ρ_e values of unknown particles based on the D_a

204 and D_{va} values. Because the AAC and SPAMS instruments have the ability to determine

205 D_a and D_{va} , the AAC-SPAMS system, which is developed in this study, can be used to

206 obtain the D_{ve} and ρ_e values for unknown particles.

207

208 **3. Results and discussion**

209 **3.1 Verification of the AAC-SPAMS system to obtain D_{ve} and ρ_e**

210 The D_{va} distribution of PSL particles with predefined D_{ve} values after screening by

211 the AAC is shown in Figure S1. We used Gaussian fitting to obtain the peak D_{va} for
212 PSL particles of predefined size with an R-squared fitting coefficient (R^2) over 0.98.
213 Each fitting has a full width at half maximum (FWHM) of 6.6%, 4.4%, 2.3% and 2.2%,
214 and the corresponding peaks are 215.8 nm, 319.0 nm, 532.1 nm and 803.5 nm,
215 respectively. Substituting the D_a and D_{va} values of PSL into Eq. (11), the measured D_{ve}
216 ($D_{ve,me}$) of PSL from AAC-SPAMS system is 203.6 nm, 309.7 nm, 511.6 nm and 737.2
217 nm, respectively (Figure 2a). Thus, the deviations between the theoretical D_{ve} ($D_{ve,th}$)
218 and $D_{ve,me}$ values are 0.3%, -0.1%, 0.3% and -0.4%, respectively. On the other hand, the
219 measured ρ_e ($\rho_{e,me}$) values of the particles are calculated from the D_{va} and $D_{ve,me}$ values
220 with Eq. (14), and the $\rho_{e,me}$ values are 1.1 g/cm³, 1.0 g/cm³, 1.0 g/cm³, and 1.1 g/cm³
221 (Figure 2b). The deviations of $\rho_{e,me}$ are determined to be 4.3%, -5.2%, -5.2%, and 4.3%,
222 respectively, by comparing to the theoretical ρ_e ($\rho_{e,th}$) that is equals to the ρ_p for the
223 spherical particles (i.e. 1.055 g/cm³ of PSL particles). That is, the deviations of $D_{ve,me}$
224 and $\rho_{e,me}$ characterized by the AAC-SPAMS system are within 1% and 6%, respectively.
225 We therefore conclude that the AAC-SPAMS system is highly accurate for obtaining
226 aerosol D_{ve} and ρ_e .

227

228 **3.2 Application of the AAC-SPAMS system for obtaining D_{ve} and ρ_e of $(\text{NH}_4)_2\text{SO}_4$** 229 **and NaNO_3**

230 Figure S2 shows the D_{va} distributions of $(\text{NH}_4)_2\text{SO}_4$ and NaNO_3 particles, which have
231 D_a values of 250.0, 350.0, 450.0, and 550.0 nm, as screened by the AAC. The D_{va} peaks
232 are obtained by Gaussian fitting, with R^2 values over 0.93 and FWHM values ranging

233 from 7.6% to 10.6%. The $(\text{NH}_4)_2\text{SO}_4$ particles have D_{va} values of 300.0, 418.0, 551.1,
234 and 695.1 nm (Figure S2), which correspond to particles possessing $D_{ve,me}$ values of
235 177.3, 254.4, 331.8, and 409.3 nm, respectively, according to Eq. (11). Substituting the
236 values of D_{va} and $D_{ve,me}$ into Eq. (12), the $\rho_{e,me}$ values are 1.7, 1.6, 1.6, and 1.7 g/cm^3
237 (Figure 3a), respectively. Similarly, the selected NaNO_3 particles are determined to
238 have D_{va} values of 321.0, 454.9, 599.8, and 755.3 nm (Figure S2), corresponding to
239 $D_{ve,me}$ values of 150.1, 218.2, 287.0, and 355.9 nm, respectively. The $\rho_{e,me}$ values of the
240 NaNO_3 particles are 2.2, 2.0, 2.0, and 2.1 g/cm^3 for the four particle sizes (Figure 3b),
241 respectively. Figure 3 also shows that the $\rho_{e,me}$ values of the NaNO_3 and $(\text{NH}_4)_2\text{SO}_4$
242 particles at four size deviate from their average values with the maximum of 5.9 % and
243 4.8%, respectively, which are identical with the deviation phenomenon for the $\rho_{e,me}$ of
244 PSL particles. These deviations may be derived from the calibration of particle D_{va}
245 from the SPAMS. While the R-square of size calibration curve is 0.999, the curve of
246 exponential function is found to slightly deviate from the data points measured by
247 SPAMS. For example, size calibration function has the deviation of -4.4% and 3.1%
248 from the data points of 310 and 740 nm, respectively.

249 Taking the systematic error into account, the slight difference of the $\rho_{e,me}$ values for
250 the four sizes suggests that the ρ_e of $(\text{NH}_4)_2\text{SO}_4$ and NaNO_3 particles is independent of
251 particle size from 250.0 nm to 550.0 nm. It is determined by the definition of effective
252 density used in this study, which keeps constant as long as the χ_a of the particles does
253 not change with particle size for pure compound. The average $\rho_{e,me}$ values of $(\text{NH}_4)_2\text{SO}_4$
254 and NaNO_3 particles are calculated to be 1.7 ± 0.1 and 2.1 ± 0.1 g/cm^3 , respectively.

255 The average $\rho_{e,me}$ values are lower than that the ρ_p of $(\text{NH}_4)_2\text{SO}_4$ (1.77 g/cm^3) and
256 NaNO_3 (2.27 g/cm^3), which is caused that the $\rho_{e,me}$ is determined by both of ρ_p and χ_a .
257 According to Eq. (14), the χ_a of $(\text{NH}_4)_2\text{SO}_4$ and NaNO_3 particles with different D_a are
258 calculated to be 1.04, 1.11, 1.11, and 1.04 and to be 1.03, 1.14, 1.14, and 1.08,
259 respectively. Thus, the average χ_a values of the $(\text{NH}_4)_2\text{SO}_4$ and NaNO_3 particles are
260 determined to be 1.07 ± 0.04 and 1.10 ± 0.05 , respectively, which can be used to
261 parameterize their morphology.

262 The average χ_a values of the $(\text{NH}_4)_2\text{SO}_4$ and NaNO_3 particles indicate that these
263 particles are aspherical. The asphericity of $(\text{NH}_4)_2\text{SO}_4$ determined by AAC-SPAMS
264 system is consistent with the previous studies reporting that the χ_a of $(\text{NH}_4)_2\text{SO}_4$ were
265 larger than the value of 1.03 (Zelenyuk et al., 2006; Beranek et al., 2012; Zhang et al.,
266 2016a). However, previous studies found that the NaNO_3 particles had different
267 morphology. Zhang et al. (2016a) observed that NaNO_3 had the χ_a of 1.09-1.13,
268 indicating its asphericity, while Hoffman et al. (2004) found that NaNO_3 particle had a
269 round droplet-like shape even at 15% RH, which was supported by the consistence
270 between the measured value of “anhydrous” droplet density and the calculated value of
271 “anhydrous” solution droplet (Zelenyuk et al., 2005). Eclectically, Tang and
272 Munkelwitz (1994) studied that most of the NaNO_3 particles crystallized between 20%
273 and 30% RH but some persisted down to 10% RH to form solution droplets. Notably,
274 the spherical NaNO_3 particles at low RH observed by Hoffman et al. (2004) were dried
275 in the sticky carbon tape which might affect the phase transition of droplet-like NaNO_3
276 particles. In this study, most NaNO_3 particles were crystallized because the RH of the

277 aerosol flow carrying the NaNO_3 particles was reduced to below 20% through the
278 diffusion drying tube. Besides, the result that the crystallized NaNO_3 particles are
279 aspherical is supported by their FWHM values of the D_{va} distributions which are
280 consistent with that of aspherical $(\text{NH}_4)_2\text{SO}_4$ but wider than spherical PSL (Figures S1
281 and S2).

282

283 **3.3 Application of the AAC-SPAMS system for measuring the chemically-resolved**

284 **D_{ve} and ρ_e**

285 SPAMS can obtain information on the chemical composition of individual particles,
286 implying that the AAC-SPAMS system has the ability to simultaneously characterize
287 D_{ve} , ρ_e and the chemical compositions of particles in real time. It is worth noting that
288 the particles with the largest χ in the actual atmosphere should be freshly emitted soot,
289 which χ is 2.5 (Peng et al., 2016). This largest χ fitly meets the upper limit for the
290 approximation between the χ_t and χ_v (DeCarlo et al., 2004). Therefore, the AAC-
291 SPAMS system can obtain the chemically-resolved D_{ve} and ρ_e values for unknown
292 aerosol particles in the field observation.

293 As an example, we applied the AAC-SPAMS system to illustrate how the measured
294 D_a , D_{va} , and chemical composition of an individual particle can be used to calculate the
295 D_{ve} and ρ_e for unknown particles. The sampled ~100,000 particles are classified into
296 eight major particle types with distinct chemical patterns of K-rich, EC-S, K-Na, Amine,
297 EC-N-S, OC-N-S and OC-EC-N-S and Metal-rich, representing 97% of the detected
298 particle population. Details of the chemical composition and number fraction of the

299 eight types of particles are presented in the Figures S3 and S4, respectively, which are
300 discussed in the Supporting Information.

301 We used Gaussian fitting to obtain the D_{va} peaks for each particle type with D_a values
302 of 250.0 nm, 350.0 nm, 450.0 nm, and 550.0 nm. Then, we calculated the D_{ve} values of
303 the atmospheric particles with Eq. (11). Table 1 presents the average D_{ve} values of the
304 eight particle types, for which the standard deviation is calculated based on nine
305 samples. The average D_{ve} at D_a values of 250.0 nm, 350.0 nm, 450.0 nm, and 550.0 nm
306 has the following wide ranges: from 188.5 nm to 200.8 nm, 271.9 nm to 295.7 nm,
307 342.5 nm to 428.9 nm, and 397.3 nm to 570.9 nm, respectively, which are caused by
308 the chemical composition differences. The result indicates that particles with
309 significantly different D_{ve} might possess the same D_a . Furthermore, the large standard
310 deviation of D_{ve} , such as 21.9 nm for K-Na at 250.0 nm, 32.3 nm for OC-EC-N-S at
311 350.0 nm, and 44.3 nm for OC-N-S at 450.0 nm, indicates that the D_{ve} of particles is
312 remarkably different even for particles with the same type and same D_a .

313 According to D_{ve} and D_{va} , we calculated the ρ_e of each particle type with Eq. (12).
314 Figure 4 shows the variations of the ρ_e with D_{ve} for nine particle samples. For pure
315 compounds, such as $(\text{NH}_4)_2\text{SO}_4$ and NaNO_3 particle, ρ_e theoretically does not change
316 with particle size. However, the sampled particles have experienced complex
317 atmospheric processes. Therefore, ρ_e has a very wide distribution for each type of
318 particle with a similar D_{ve} . Specifically, the ρ_e of K-Na increases with D_{ve} , while the ρ_e
319 of OC-N-S and OC-EC-N-S decreases with D_{ve} , which may be influenced by the
320 particle shape or the material density. Additionally, the average ρ_e of each type of

321 particle is in the order from small to large: $1.2 \pm 0.2 \text{ g/cm}^3$ for OC-EC-N-S, 1.3 ± 0.2
322 g/cm^3 for OC-N-S, $1.4 \pm 0.1 \text{ g/cm}^3$ for K-rich, $1.4 \pm 0.1 \text{ g/cm}^3$ for Amine, 1.5 ± 0.1
323 g/cm^3 for EC-N-S, $1.5 \pm 0.1 \text{ g/cm}^3$ for EC-S, $1.6 \pm 0.1 \text{ g/cm}^3$ for K-Na and 1.6 ± 0.1
324 g/cm^3 for Metal-rich. It is reasonable to find that the average ρ_e of internally mixed
325 particles distributes in the range of their material densities (ρ_m). For instance, mainly
326 comprised of internally mixed sulfate and organics, the OC-EC-N-S, OC-N-S, K-rich,
327 and Amine particles have the average ρ_e between that of sulfate with ρ_m of 1.77 g/cm^3
328 and organic aerosols with ρ_m of 1.2 g/cm^3 (Cross et al., 2007).

329

330 **4. Conclusion**

331 We first develop an AAC-SPAMS system to achieve the measurement of the D_{ve} and
332 ρ_e of the particles through characterizing their D_a and D_{va} . The reliability of the AAC-
333 SPAMS system is verified by accurately measuring the D_{ve} and ρ_e of PSL. Applying the
334 AAC-SPAMS system to determine the D_{ve} and ρ_e of $(\text{NH}_4)_2\text{SO}_4$ and NaNO_3 particles
335 shows that these particles are aspherical and their ρ_e are independent of particle size.
336 Coupled with the ability of SPAMS to characterize the chemical composition of
337 individual particles, we conducted a sample proof of the AAC-SPAMS equipment to
338 first simultaneously characterize the D_{ve} , ρ_e and chemical compositions of atmospheric
339 particles, showing the potential application of this system in field observations. The
340 approach achieves the measurement of chemically-resolved D_{ve} and ρ_e , and provides
341 the possibility to determine their quantitative relationship with other particle properties,
342 which would be benefit for further reduction of the uncertainty associated with the

343 effects of particles on air quality, human health and radiative forcing.

344

345 **Data availability.** Data in this study is available at [https://github.com/longer1217/All-](https://github.com/longer1217/All-figures-data)
346 figures-data.

347

348 **Author contributions.** The idea for the study was conceived by LP and GHZ. All
349 experiments were performed by LP with the assistance of LL. LP wrote the paper which
350 was reviewed by GHZ and XHB. All co-authors discussed the results and commented
351 on the manuscript.

352

353 **Competing interests.** The authors declare they have no conflict of interest.

354

355 **Acknowledgment**

356 This work was supported by the National Nature Science Foundation of China
357 (41775124 and 41877307), Natural Science Foundation of Guangdong Province
358 (2019B151502022), and the Guangdong Foundation for the Program of Science and
359 Technology Research (2019B121205006 and 2017B030314057). The authors also
360 gratefully acknowledge Cambustion Ltd., UK for providing the AAC and Hexin
361 Analytical Instrument Co., Ltd., China for providing the SPAMS.

362

363 **References**

364 Alexander, J. M., Bell, D. M., Imre, D., Kleiber, P. D., Grassian, V. H., and Zelenyuk,

365 A.: Measurement of size-dependent dynamic shape factors of quartz particles in
366 two flow regimes, *Aerosol Sci. and Technol.*, 50, 870-879,
367 <https://doi.org/10.1080/02786826.2016.1200006>, 2016.

368 Beranek, J., Imre, D., and Zelenyuk, A.: Real-time shape-based particle separation and
369 detailed in situ particle shape characterization, *Anal. Chem.*, 84, 1459-1465,
370 <https://doi.org/10.1021/ac202235z>, 2012.

371 Buseck, P. R., and Posfai, M.: Airborne minerals and related aerosol particles: effects
372 on climate and the environment, *P. Natl. Acad. Sci. USA*, 96, 3372-3379,
373 <https://doi.org/10.1073/pnas.96.7.3372>, 1999.

374 Cross, E. S., Slowik, J. G., Davidovits, P., Allan, J. D., Worsnop, D. R., Jayne, J. T.,
375 Lewis, D. K., Canagaratna, M., and Onasch, T. B.: Laboratory and ambient particle
376 density determinations using light scattering in conjunction with aerosol mass
377 spectrometry, *Aerosol Sci. and Technol.*, 41, 343-359,
378 <https://doi.org/10.1080/02786820701199736>, 2007.

379 DeCarlo, P. F., Slowik, J. G., Worsnop, D. R., Davidovits, P., and Jimenez, J. L.: Particle
380 morphology and density characterization by combined mobility and aerodynamic
381 diameter measurements. Part 1: Theory, *Aerosol Sci. and Technol.*, 38, 1185-1205,
382 <https://doi.org/10.1080/027868290903907>, 2004.

383 Dinar, E., Mentel, T. F., and Rudich, Y.: The density of humic acids and humic like
384 substances (HULIS) from fresh and aged wood burning and pollution aerosol
385 particles, *Atmos. Chem. Phys.*, 6, 5213-5224, <https://doi.org/10.5194/acp-6-5213->
386 2006, 2006.

387 Guo, S., Hu, M., Zamora, M. L., Peng, J. F., Shang, D. J., Zheng, J., Du, Z. F., Wu, Z.,
388 Shao, M., Zeng, L. M., Molina, M. J., and Zhang, R. Y.: Elucidating severe urban
389 haze formation in China, *P. Natl. Acad. Sci. USA*, 111, 17373-17378, 2014.

390 Han, C., Li, S. M., Liu, P., and Lee, P.: Size dependence of the physical characteristics
391 of particles containing refractory black carbon in diesel vehicle exhaust, *Environ.*
392 *Sci. & Technol.*, 53, 137-145, <https://doi.org/10.1021/acs.est.8b04603>, 2019.

393 Hand, J. L., and Kreidenweis, S. M.: A new method for retrieving particle refractive
394 index and effective density from aerosol size distribution data, *Aerosol Sci. and*
395 *Technol.*, 36, 1012-1026, <https://doi.org/10.1080/02786820290092276>, 2002.

396 Hoffman, R. C., Laskin, A., and Finlayson-Pitts, B. J.: Sodium nitrate particles:
397 physical and chemical properties during hydration and dehydration, and
398 implications for aged sea salt aerosols, *J. Aerosol Sci.*, 35, 869-887, 2004.

399 Katrib, Y., Martin, S. T., Rudich, Y., Davidovits, P., Jayne, J. T., and Worsnop, D. R.:
400 Density changes of aerosol particles as a result of chemical reaction, *Atmos. Chem.*
401 *Phys.*, 5, 275-291, <https://doi.org/10.5194/acp-5-275-2005>, 2005.

402 Kiselev, A., Wennrich, C., Stratmann, F., Wex, H., Henning, S., Mentel, T. F., Kiendler-
403 Scharr, A., Schneider, J., Walter, S., and Lieberwirth, I.: Morphological
404 characterization of soot aerosol particles during LACIS Experiment in November
405 (LExNo), *J. Geophys. Res.-Atmos.*, 115, Artn D11204.
406 <https://doi.org/10.1029/2009jd012635>, 2010.

407 Li, L., Huang, Z. X., Dong, J. G., Li, M., Gao, W., Nian, H. Q., Fu, Z., Zhang, G. H.,
408 Bi, X. H., Cheng, P., and Zhou, Z.: Real time bipolar time-of-flight mass

409 spectrometer for analyzing single aerosol particles, *Int. J. Mass Spectrom.*, 303,
410 118-124, <https://doi.org/10.1016/j.ijms.2011.01.017>, 2011.

411 Liu, Y., and Daum, P. H.: Relationship of refractive index to mass density and self-
412 consistency of mixing rules for multicomponent mixtures like ambient aerosols, *J.*
413 *Aerosol Sci.*, 39, 974-986, <https://doi.org/10.1016/j.jaerosci.2008.06.006>, 2008.

414 Liu, Z., Hu, B., Ji, D., Wang, Y., Wang, M., and Wang, Y.: Diurnal and seasonal
415 variation of the PM_{2.5} apparent particle density in Beijing, China, *Atmos.*
416 *Environ.*, 120, 328-338, <https://doi.org/10.1016/j.atmosenv.2015.09.005>, 2015.

417 Moffet, R. C., and Prather, K. A.: Extending ATOFMS measurements to include
418 refractive index and density, *Anal. Chem.* 77, 6535-6541,
419 <https://doi.org/10.1021/ac0503097>, 2005.

420 Moffet, R. C., Qin, X., Rebotier, T., Furutani, H., and Prather, K. A.: Chemically
421 segregated optical and microphysical properties of ambient aerosols measured in
422 a single-particle mass spectrometer, *J. Geophys. Res.-Atmos.*, 113,
423 <https://doi.org/10.1029/2007jd009393>, 2008.

424 Peng, J. F., Hu, M., Guo, S., Du, Z. F., Zheng, J., Shang, D. J., Zamora, M., Zeng, L.
425 M., Shao, M., Wu, Y. S., Zheng, J., Wang, Y., Glen, C., Collins, D., Molina, M.,
426 and Zhang, R. Y.: Markedly enhanced absorption and direct radiative forcing of
427 black carbon under polluted urban environments, *P. Natl. Acad. Sci. USA*, 252,
428 2016.

429 Pitz, M., Cyrys, J., Karg, E., Wiedensohler, A., Wichmann, H. E., and Heinrich, J.:
430 Variability of apparent particle density of an urban aerosol, *Environ. Sci. &*

431 Technol., 37, 4336-4342, <https://doi.org/10.1021/es034322p>, 2003.

432 Poschl, U.: Atmospheric aerosols: Composition, transformation, climate and health
433 effects, *Angew. Chem. Int. Edit.*, 44, 7520-7540,
434 <https://doi.org/10.1002/anie.200501122>, 2005.

435 Schneider, J., Weimer, S., Drewnick, F., Borrmann, S., Helas, G., Gwaze, P., Schmid,
436 O., Andreae, M. O., and Kirchner, U.: Mass spectrometric analysis and
437 aerodynamic properties of various types of combustion-related aerosol particles,
438 *Int. J. Mass Spectrom.*, 258, 37-49, <https://doi.org/10.1016/j.ijms.2006.07.008>,
439 2006.

440 Seinfeld, J. H., and Pandis, S. N.: From air pollution to climate change, 429-443, 1998.

441 Song, X. H., Hopke, P. K., Ferguson, D. P., and Prather, K. A.: Classification of single
442 particles analyzed by ATOFMS using an artificial neural network, ART-2A, *Anal.*
443 *Chem.*, 71, 860-865, <https://doi.org/10.1021/ac9809682>, 1999.

444 Spencer, M. T., and Prather, K. A.: Using ATOFMS to determine OC/EC mass fractions
445 in particles, *Aerosol Sci. and Technol.*, 40, 585-594,
446 <https://doi.org/10.1080/02786820600729138>, 2006.

447 Spencer, M. T., Shields, L. G., and Prather, K. A.: Simultaneous measurement of the
448 effective density and chemical composition of ambient aerosol particles, *Environ.*
449 *Sci. & Technol.*, 41, 1303-1309, <https://doi.org/10.1021/es061425+>, 2007.

450 Sumlin, B. J., Oxford, C. R., Seo, B., Pattison, R. R., Williams, B. J., and Chakrabarty,
451 R. K.: Density and homogeneous internal composition of primary brown carbon
452 *Aerosol, Environ. Sci. & Technol.*, 52, 3982-3989,

453 <https://doi.org/10.1021/acs.est.8b00093>, 2018.

454 Tang, I. N., and Munkelwitz, H. R.: Water activities, densities, and refractive-indexes
455 of aqueous sulfates and sodium-nitrate droplets of atmospheric importance, *J.*
456 *Geophys. Res.-Atmos.*, 99, 18801-18808, 1994.

457 Tang, I. N.: Thermodynamic and optical properties of mixed-salt aerosols of
458 atmospheric importance, *J. Geophys. Res.-Atmos.*, 102, 1883-1893, 1997.

459 Tavakoli, F., and Olfert, J. S.: An instrument for the classification of aerosols by particle
460 relaxation time: theoretical models of the aerodynamic aerosol classifier, *Aerosol*
461 *Sci. and Technol.*, 47, 916-926, <https://doi.org/10.1080/02786826.2013.802761>,
462 2013.

463 Wu, Y. F., Xia, Y. J., Huang, R. J., Deng, Z. Z., Tian, P., Xia, X. G., and Zhang, R. J.: A
464 study of the morphology and effective density of externally mixed black carbon
465 aerosols in ambient air using a size-resolved single-particle soot photometer (SP2),
466 *Atmos. Meas. Tech.*, 12, 4347-4359, 2019.

467 Yin, Z., Ye, X. N., Jiang, S. Q., Tao, Y., Shi, Y., Yang, X., and Chen, J. M.: Size-resolved
468 effective density of urban aerosols in Shanghai, *Atmos. Environ.*, 100, 133-140,
469 <https://doi.org/10.1016/j.atmosenv.2014.10.055>, 2015.

470 Yon, J., Bescond, A., and Ouf, F. X.: A simple semi-empirical model for effective
471 density measurements of fractal aggregates, *J. Aerosol Sci.*, 87, 28-37,
472 <https://doi.org/10.1016/j.jaerosci.2015.05.003>, 2015.

473 Zelenyuk, A., Cai, Y., Chieffo, L., and Imre, D.: High precision density measurements
474 of single particles: The density of metastable phases, *Aerosol Sci. and Technol.*,

475 39, 972-986, <https://doi.org/10.1080/02786820500380206>, 2005.

476 Zelenyuk, A., Cai, Y., and Imre, D.: From agglomerates of spheres to irregularly shaped
477 particles: Determination of dynamic shape factors from measurements of mobility
478 and vacuum aerodynamic diameters, *Aerosol Sci. and Technol.*, 40, 197-217,
479 <https://doi.org/10.1080/02786820500529406>, 2006.

480 Zhai, J. H., Lu, X. H., Li, L., Zhang, Q., Zhang, C., Chen, H., Yang, X., and Chen, J.
481 M.: Size-resolved chemical composition, effective density, and optical properties
482 of biomass burning particles, *Atmos. Chem. Phys.*, 17, 7481-7493,
483 <https://doi.org/10.5194/acp-17-7481-2017>, 2017.

484 Zhang, G., Bi, X., Han, B., Qiu, N., Dai, S., Wang, X., Sheng, G., and Fu, J.:
485 Measurement of aerosol effective density by single particle mass spectrometry,
486 *Science China Earth Sciences*, 59, 320-327, [https://doi.org/10.1007/s11430-015-](https://doi.org/10.1007/s11430-015-5146-y)
487 5146-y, 2016a.

488 Zhang, Y. X., Zhang, Q., Cheng, Y. F., Su, H., Kecorius, S., Wang, Z. B., Wu, Z. J., Hu,
489 M., Zhu, T., Wiedensohler, A., and He, K. B.: Measuring the morphology and
490 density of internally mixed black carbon with SP2 and VTDMA: new insight into
491 the absorption enhancement of black carbon in the atmosphere, *Atmos. Meas.*
492 *Tech.*, 9, 1833-1843, <https://doi.org/10.5194/amt-9-1833-2016>, 2016b.

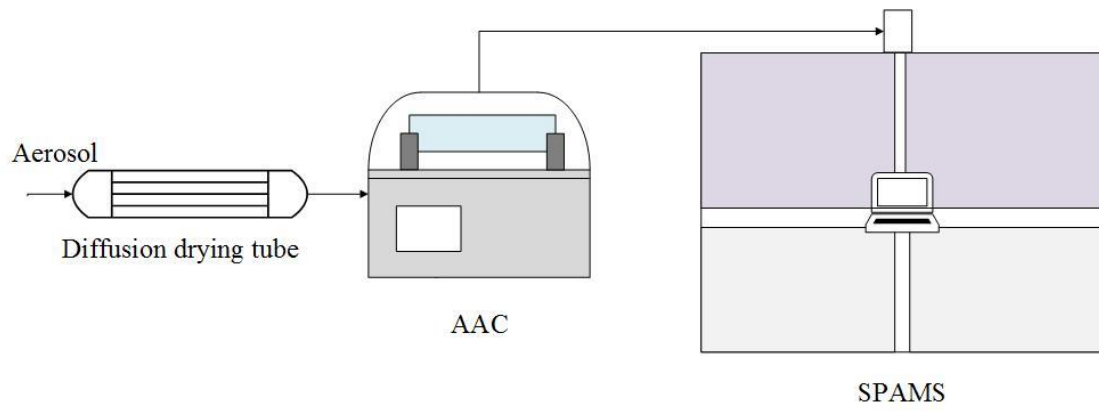
493 Zhao, G., Zhao, W., and Zhao, C.: Method to measure the size-resolved real part of
494 aerosol refractive index using differential mobility analyzer in tandem with single-
495 particle soot photometer, *Atmos. Meas. Tech.*, 12, 3541-3550,
496 <https://doi.org/10.5194/amt-12-3541-2019>, 2019.

498 **Table 1.** The measured mean D_{ve} and its standard deviation for the eight particle types at D_a values
 499 of 250.0 nm, 350.0 nm, 450.0 nm, and 550.0 nm from nine round measurement.
 500

D_a (nm)	K-rich	EC-S	K-Na	Amine
250.0	193.1 ± 8.2	192.2 ± 8.1	193.8 ± 21.9	190.6 ± 4.6
350.0	284.0 ± 28.4	280.8 ± 9.3	271.9 ± 18.0	284.8 ± 18.2
450.0	364.7 ± 21.1	357.8 ± 6.9	342.5 ± 7.3	367.9 ± 9.7
550.0	416.6 ± 28.3	439.5 ± 5.4	397.3 ± 29.7	442.5 ± 7.4
D_a (nm)	EC-N-S	OC-N-S	OC-EC-N-S	Metal-rich
250.0	188.5 ± 5.9	200.8 ± 17.9	195.4 ± 8.9	189.0 ± 6.7
350.0	281.3 ± 9.3	295.7 ± 29.8	294.0 ± 32.3	277.0 ± 9.1
450.0	358.0 ± 5.8	398.3 ± 44.3	428.9 ± 24.0	342.9 ± 10.0
550.0	453.2 ± 16.4	547.4 ± 14.7	570.9	407.4 ± 14.5

501

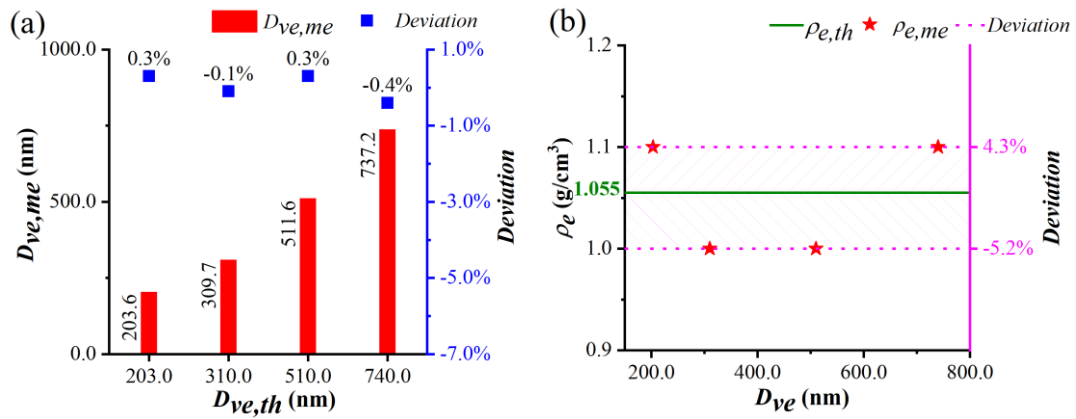
502



503

504 **Figure 1.** Schematic diagram of the AAC-SPAMS system (0.3 lpm). The diffusion drying tube is

505 filled with orange silica gel, which reduces the RH to 5-15%.



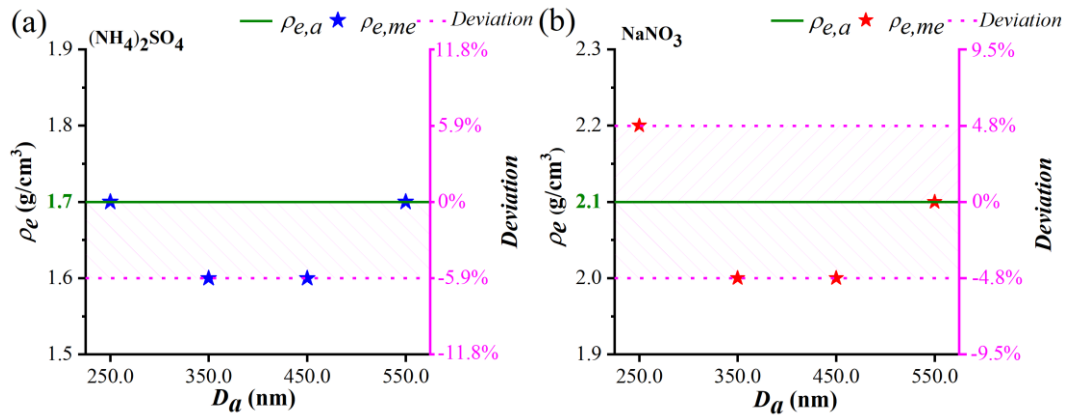
506

507

508 **Figure 2.** (a) Comparison between the measured D_{ve} ($D_{ve,me}$) and the theoretical D_{ve} ($D_{ve,th}$) of the

509 PSL particles. (b) Comparison between the measured ρ_e ($\rho_{e,me}$) and the theoretical ρ_e ($\rho_{e,th}$) of the

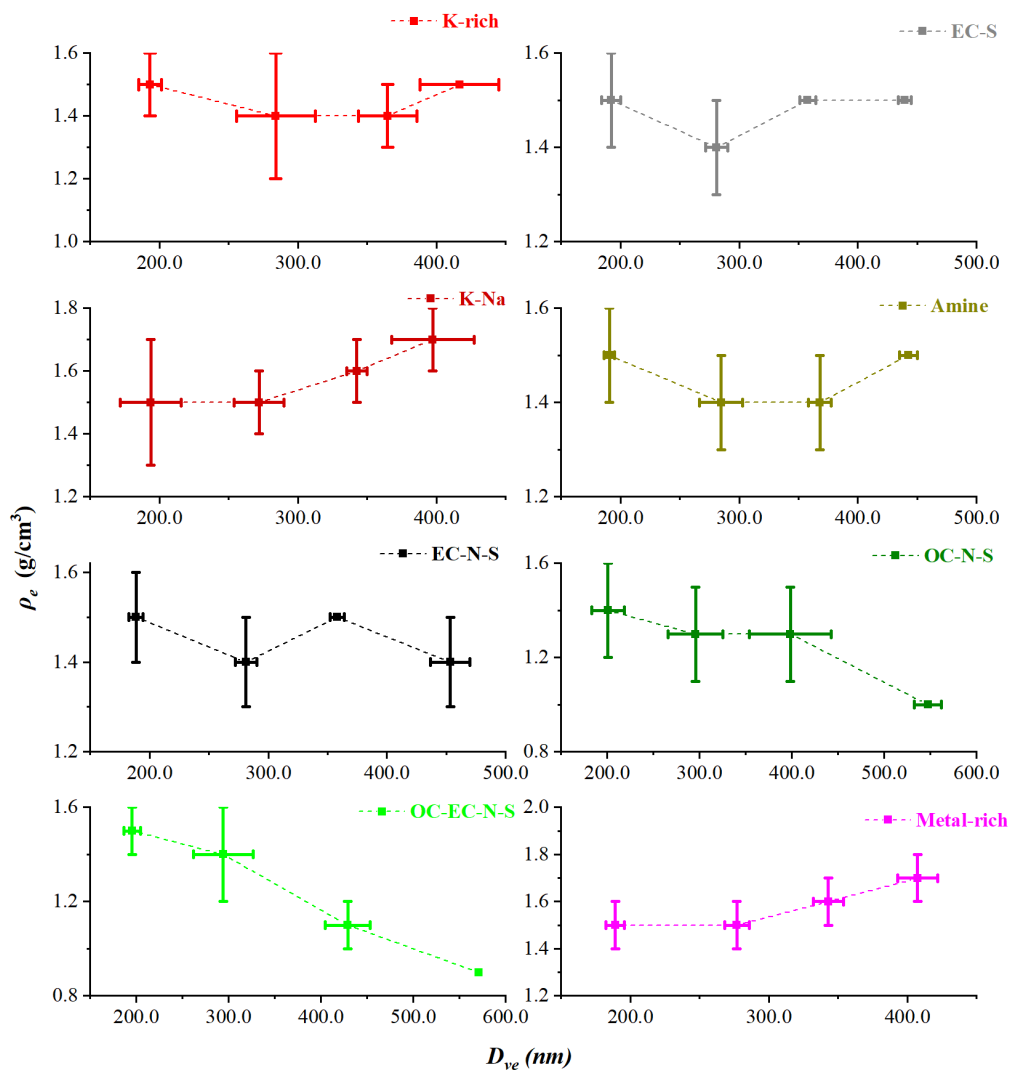
510 PSL particles.



511

512

513 **Figure 3.** (a) Comparison between the measured ρ_e ($\rho_{e,me}$) and average ρ_e ($\rho_{e,a}$) values of the
 514 $(\text{NH}_4)_2\text{SO}_4$ particles. (b) Comparison between the measured ρ_e ($\rho_{e,me}$) and average ρ_e ($\rho_{e,a}$) values of
 515 the NaNO_3 particles.



516

517

518 **Figure 4.** Variation in ρ_e of the eight particle types with D_{ve} . The solid lines represent the rang of

519 the ρ_e and D_{ve} measured from nine rounds, and the data points stand for the average values.